

The spectral upwelling radiance distribution in optically shallow waters

Kenneth J. Voss¹

Physics Department, University of Miami, Coral Gables, Florida, 33143

Curtis D. Mobley and Lydia K. Sundman

Sequoia Scientific, Incorporated, Westpark Technical Center, 15317 Northeast 90th Street, Redmond, Washington 98052

James E. Ivey

College of Marine Science, University of South Florida, 140 7th Avenue South, St. Petersburg, Florida, 33701

Charles H. Mazel

Physical Sciences Incorporated, 20 New England Business Center, Andover, Massachusetts 01810

Abstract

The upwelling radiance distribution in optically shallow water is investigated with experiments and Hydrolight numerical simulations for two different benthic surfaces and a range of solar zenith angles ($<60^\circ$). Over a bright sand surface (water depth 5 m) the upwelling radiance distribution was brightest at nadir and decreased toward the horizon. The upwelling radiance distribution was nearly azimuthally symmetric but was strongly influenced by wave focusing. Q (E_u/L_u , where E_u is the upwelling irradiance and L_u is the upwelling radiance) for this case was significantly less than π . Q , at 440 nm and 670 nm, was almost independent of solar zenith angle. The Hydrolight model results agreed well with the experimental measurements in this case. Over a seagrass surface (water depth 8 m) at 440 nm the radiance distribution was more uniform, while at 670 nm the benthic surface has a negligible effect on the upwelling radiance distribution. In this case, Q was dependent on solar zenith angle, with $Q(670\text{ nm})$ close to the values expected in optically deep water. At 440 nm, the agreement between the radiance distribution obtained from Hydrolight and the data is better at larger solar zenith angles, but at small solar zenith angles the experiments indicated that there were significant non-Lambertian effects over the seagrass surface, with a much higher reflectance at small nadir view angles.

In optically shallow water the light reflected from the benthic surface affects the remotely sensed water leaving radiance. Many workers have developed models that account for the effect of the benthic surface on the upwelling irradiance field (e.g., Joseph 1950; Plass and Kattawar 1972; Gordon and Brown 1974; Maritorena et al. 1994) and nadir upwelling radiance (Lee et al. 1998). However, most often the remotely sensed signal is not at nadir, but at some other viewing angle. In this case the variation of the upwelling radiance with view angle is required.

The radiance distribution is the collection of information on the angular variation of the radiance in the ambient light field. In optically shallow water, reflectance from the benthic surface will modify the radiance distribution from that expected in optically deep water. Thus to understand remote sensing in shallow waters, we need to understand the effect of the benthic surface on the radiance distribution. The radiance distribution also provides a very detailed data set to

study closure with radiative transfer models. To study these effects, two series of upwelling radiance distribution measurements were made with contrasting benthic surfaces in shallow (5–8 m) water.

The experiments were performed in the Exuma Islands, Bahamas near Lee Stocking Island and the Caribbean Marine Research Center. The two benthic surfaces chosen were a bright white sand surface and a seagrass bed. In each case a large area was selected that was as homogeneous as possible. At each location measurements were made at various solar zenith angles (θ_s) throughout the day, to investigate the effect of incident angle on the upwelling radiance distribution. Associated measurements were made of the benthic reflectance and water column inherent optical properties (spectral light absorption, $a(\lambda)$, and spectral beam attenuation, $c(\lambda)$). Simulations of the experiment were performed using the Hydrolight 4.1 radiative transfer numerical model (Mobley et al. 1993; Mobley 1994; Mobley and Sundman 2001a,b) and the semianalytic model of Lee et al. (1999). Comparisons of the simulations and model with the data aid in understanding how the radiance distribution is formed.

Methods

Radiance distribution measurements—Measurements of the upwelling radiance distribution were made using the RADS-II radiance distribution camera system (Voss 1989;

¹ Corresponding author (voss@physics.miami.edu).

Acknowledgments

This work was supported by the Environmental Optics program at the Office of Naval Research as part of the Coastal Benthic Optical Properties (CoBOP) research initiative. We would also like to thank the crew of the R/V *Subchaser* (David Costello and Tom Peacock) and Albert L. Chapin for their help in collecting these data.

Voss and Chapin 1992). This system is based on the use of fisheye optics that allow an entire hemisphere of radiance data to be collected in a single image (Smith et al. 1970). The RADS-II instrument has separate cameras to image the upwelling and downwelling radiance distribution; however, in this experiment only the upwelling radiance distribution was measured. Use of a filterwheel in the optical stream enables the radiance distribution to be collected in specific spectral bands. We present data from two spectral bands (440 nm and 670 nm).

In normal deep-water use of RADS, the instrument is either supported by a cable from the ship or beneath a surface float that enables it to float away from the ship and the associated ship shadow. Because we were working in such shallow, calm water we wanted the instrument closer to the surface. In this experiment an automobile tire innertube was placed around the middle of the instrument. In this way the upwelling measurement was made at approximately 75 cm below the surface. While the innertube increased the effective diameter of the instrument, it also decreased the effective length of the instrument (by removing the surface float) so instrument self-shadowing effects were offset to some extent. RADS was deployed from the Univ. S. Florida vessel, R/V *Subchaser*. The instrument was tethered approximately 15 m from the small vessel so that ship shadowing effects were negligible. The ship allowed simultaneous use of RADS and a profiling optical package to measure in situ optical parameters. Water depth estimates were obtained from the shipboard depth sounder.

The integration times for the RADS camera image varied with wavelength and benthic surface. During the sand closure experiment, exposure times for the 440-nm images were approximately 0.08 s, while the exposure times for the 670-nm measurements varied between 0.1 and 1 s. For the seagrass closure experiments, the exposure times were longer, 0.5 s for the 440-nm images and 10 s for the 670-nm images.

In situ optical properties measurements—In situ inherent optical properties were measured with a drop package. This package supported many instruments; however, we will only report and use the ac-9 from this package. The Wet Labs ac-9 measured attenuation and absorption of all constituents other than pure water at wavelengths of 412, 440, 488, 510, 532, 555, 650, 676, and 715 nm. The instrument was calibrated with purified water from a Milli-Q deionization system. The instrument deployment and data processing were in accordance with the manufacturer's recommended protocols (Wet Labs 2000).

Measurements of the benthic spectral reflectance were made using a diver operated spectrometer. The unit used was an updated version of the one described in Mazel (1997). Dubbed the DiveSpec, the instrument has a measurement probe head connected to the instrument housing by an electrical cable and a liquid light guide. The probe head contains a light source and a liquid light guide, while the instrument housing holds the spectrometer, computer, nonvolatile flash memory, and liquid crystal display (LCD). Reflectance measurements are made by first recording the light reflected from a Spectralon reference standard, then from the sample of interest, and computing the ratio.

Measurements can be made using either ambient light or an array of blue, white, and red LEDs in the probe head, which in combination provide illumination from approximately 390 to 800 nm. In the latter case the light passes through a 20° collimator and illuminates the sample at approximately normal incidence. The light guide penetrates the probe circumference and is directed at the center of the illuminated area at a 45° angle. The effective measurement area is approximately 1 cm². The collected light is conducted back to the spectrometer in the instrument housing and the data are logged in flash memory.

The probe head excludes ambient light when it is placed over a surface. This can be desirable to avoid errors associated with short-term changes in ambient illumination associated with effects such as wave focusing or the passage of clouds over the sun in the time between making the reference and sample measurements. The probe and its light source were used for the measurement of sand reflectance. For the seagrass site, the probe was not used because the small sample area would not effectively record the light reflected from a surface that is a composite of many seagrass blades against a sand background. At this site the reference was the downwelling irradiance, measured by directing the light guide at a Spectralon surface held parallel to the bottom at a height of 40 cm above the bottom. The light guide was then directed at the seagrass from the same height, at a 45° angle to make the sample measurement.

The measured parameter is really the 0°–45° (incident received) reflectance. The reflectance factor is the measured reflectance normalized to the value measured for a perfectly white diffuse reflector. If a surface is a Lambertian reflector, then the reflectance factor as measured here with the 0°–45° geometry equals the irradiance reflectance $R = E_u/E_d$ (upwelling irradiance, E_u , and downwelling irradiance, E_d), as would be measured by plane irradiance sensors located just above the sample. At normal incidence, sand is nearly Lambertian (Zhang et al. 2003). We therefore used the measured reflectance factor values as the input to Hydrolight to specify R of the assumed Lambertian sand surface. As will be seen, the assumption that seagrass is a Lambertian reflector is not supported by the observations. Nevertheless, we also assumed the seagrass to be a Lambertian reflector with R values equal to the measured reflectance factor. Correcting this inaccuracy would require measuring the bidirectional reflectance distribution function (BRDF) of the seagrass canopy. If the full BRDF were known, it could be used in Hydrolight to specify the bottom boundary condition (Mobley et al. 2003).

Hydrolight simulations—Hydrolight numerical simulations were made using water inherent optical properties, bottom reflectances, and environmental conditions approximating the conditions during the experiment. Hydrolight was run in its single-component mode using the measured total (water plus dissolved substances plus particles) inherent optical properties as input. The scattering phase function was not measured; therefore, we used two phase functions for comparison of phase function effects. The first (referred to as AUTEK in this paper) was measured by Petzold (1972; see also table 3.10 of Mobley 1994) in clear ocean waters (at

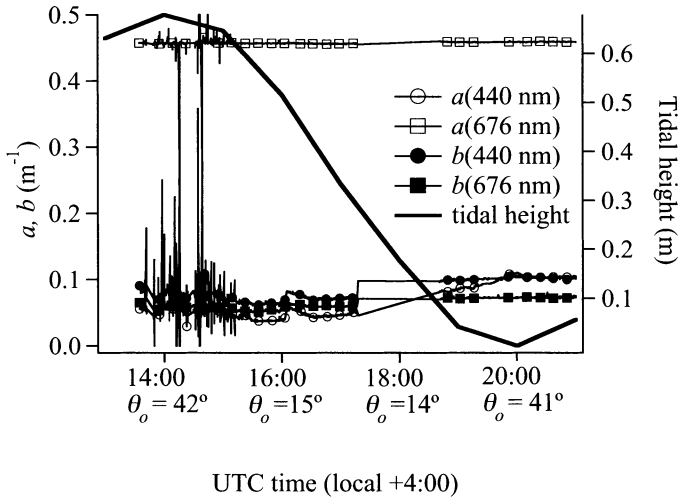


Fig. 1. Water column inherent optical properties during the bright sand measurement (20 May 2000) derived from the ac-9 package. After 1800 UTC there was an increase in the inherent optical properties through the rest of the day. The noisy portions early in the day were thought to be caused by large particles caught up in the ac-9. Also shown on this graph is the tidal height at a nearby tidal station (Settlement Point, Bahamas, http://www.co-ops.nos.noaa.gov/data_res.html).

the AUTECH site in the Bahamas); this phase function has a backscatter fraction of 0.044. The second phase function (referred to as AVG in this paper) was an average particle phase function (Mobley et al. 1993; see also table 3.10 of Mobley 1994), which has a backscatter fraction of 0.018. Input sky radiances were computed using atmospheric submodels within Hydrolight. The atmospheric parameters (aerosol type, precipitable water, ozone concentration, etc.) needed to

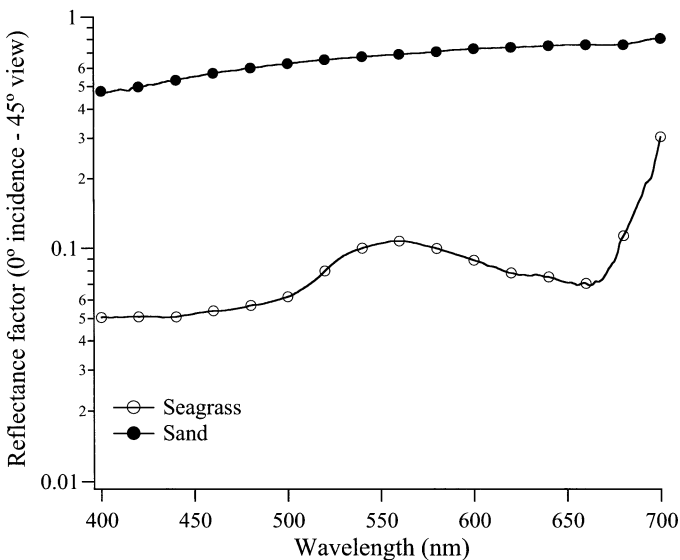


Fig. 2. Reflectance factor from Dive Spec (Mazel 1997). Filled circles are the sand reflectance, open circles are the reflectance 40 cm above the seagrass bed. This reflectance factor is the radiance reflectance compared to a 99% reflecting Spectralon plaque viewed at 45° nadir angle with the same irradiance illumination.

run the atmospheric submodels were not measured; climatological values and best guesses therefore were used to define the atmosphere. All measurements were taken in clear sky conditions. The bottom boundary condition for Hydrolight was assumed to be a Lambertian reflecting surface with R taken from measurements for the sand or seagrass at the appropriate wavelengths. The wind speed was taken to be 5 m s^{-1} .

Results

We will discuss the sand and seagrass experiments separately because there are significant differences between the two cases.

Bright sand case—This experiment was performed on 20 May 2000, at the sand closure site in North Rainbow Gardens (23°47.51'N, 76°08.33'W). The water depth was approximately 5 m at this site, and the tidal range over the day was small (approximately 0.6 m). However, the site was in a channel, so that the tidal current was significant (approximately 0.4 m s^{-1} peak). The channel led from Exuma Sound, a source of relatively clear water, to a large area of flats, which had higher levels of dissolved organics (CDOM) and other colored materials. Thus the optical properties at the site depended on the stage of the tidal current. In Fig. 1, the inherent optical properties through the day are displayed for two disparate wavelengths. Early in the day (before local noon, 1600 UTC) the optical properties were fairly constant. The large variations in the ac-9 measurements were due to large particles passing through the instrument. In the afternoon $a(440 \text{ nm})$ increased significantly (100%), but $a(670 \text{ nm})$ increased only slightly (<3%). The current at this time was ebbing; thus high CDOM values were being transported through our site from the flats to Exuma Sound. CDOM absorbs strongly in the blue, but not in the red, which accounts for the increase in $a(440 \text{ nm})$ but not $a(670 \text{ nm})$ (Jerlov 1976). The $b(\lambda)$ showed much less variation, increasing by 20% at 440 nm and 15% at 676 nm.

Figure 2 shows the measured 0°–45° (incident received) reflectance factor of the sand and seagrass. The sand reflectance is a smooth function of wavelength increasing toward the red wavelengths; the reflectance is nominally greater than 0.5 at the two wavelengths of interest here.

Figure 3 shows an example radiance distribution at 440 nm, $\theta_o = 55^\circ$, 1301 UTC. In this figure the circle is an image of the radiance distribution presented as a fisheye projection: the center of the circle is at nadir (directly upwelling), and nadir view angle, θ_v , is directly proportional to the radius from the center. The image is in absolute radiance units; a color bar is provided along with contours at integral values of radiance. The edge of the circle is at $\theta_v = 85^\circ$. There are three artifacts near the edge (two big ones on the left and right, one small one near the top), which are instrument stands that help protect the instrument window and dome.

The main features of all the sand radiance distributions are illustrated in this figure. First, the upwelling radiance distribution is dominated by the reflectance from the benthic surface. The center of the image is the brightest part, with the radiance decreasing toward the horizon. In optically deep

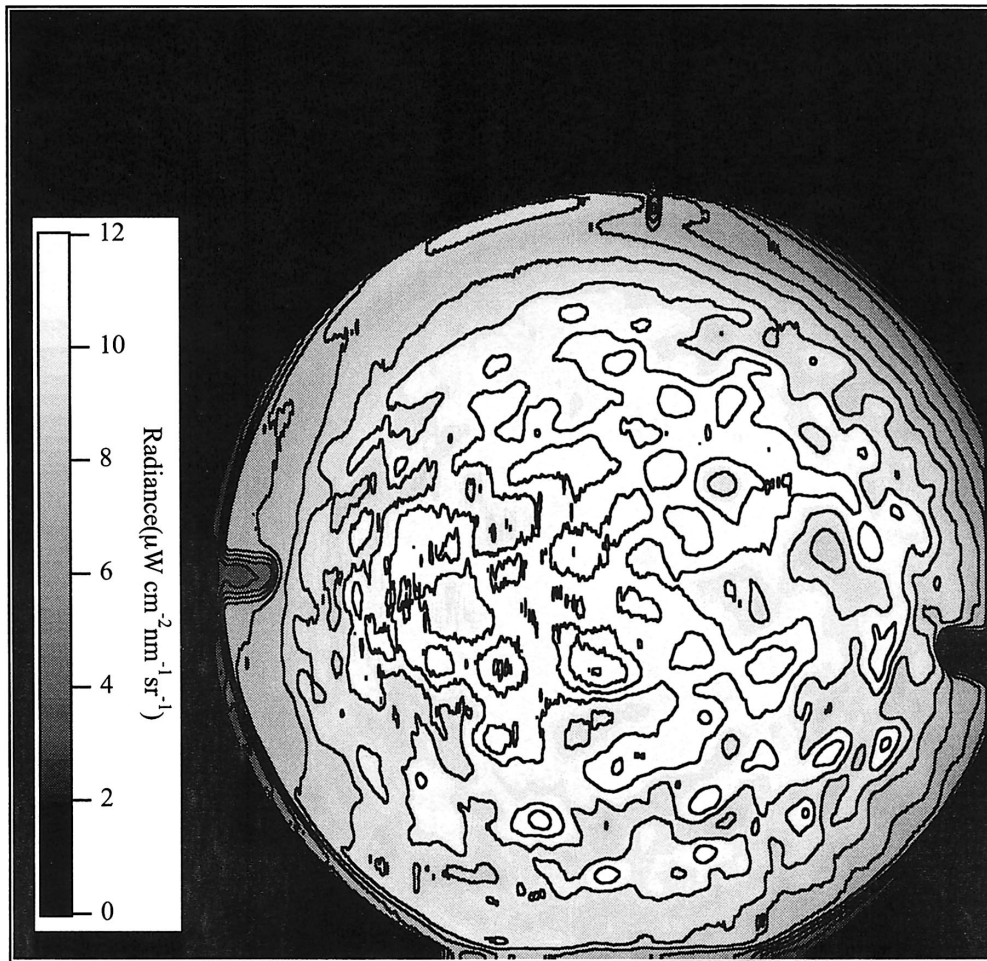


Fig. 3. A sample radiance distribution at 440 nm, $\theta_o = 55^\circ$, 1301 UTC. The figure is a fish-eye projection: the center of the circle is at nadir (directly upwelling) and θ_v is directly proportional to the radius from the center. The image is in absolute radiance units; a gray scale is provided along with contours at integral values of radiance. The edge of the circle is at $\theta_v = 85^\circ$.

water (where the benthic surface has no influence on the light field) the upwelling radiance distribution tends to increase toward the horizon rather than decrease. In these shallow waters the decrease toward the horizon is caused by the increase in pathlength between the surface sensor and the bright benthic surface that acts as an extended source of light. We will discuss this further below. The other dominant feature is the bright and dark patterns on the nearly homogeneous bottom caused by the wave focusing. This effect is easily observable in shallow water or swimming pools. The bright spots are randomly oriented and not aligned with the sand waves that exist on the benthic surface (and were obvious to divers near the surface). Thus this effect must be due to surface waves and not a BRDF effect. While this effect is obvious in our images, a remote sensing device that averages over many square meters, or over a longer time period, would average over these bright and dark spots (Zaneveld and Boss 2003).

Following the derivation by Preinsendorfer (1976) (but separating the path radiance into two portions) the upwelling

radiance distribution can be simplified into three components:

$$L_{\text{total}} = L_{\text{bottom}} + L_{\text{bottom}}^* + L_{\text{surface}}^* \quad (1)$$

These three components are the light reflected off of the benthic surface and transmitted directly to the detector (L_{bottom}), the path radiance due to light that has been reflected from the benthic surface (L_{bottom}^*), and finally the path radiance due to light that has not interacted with the benthic surface (L_{surface}^*). For a Lambertian surface, L_{bottom} can be easily written as

$$L_{\text{bottom}} = \left[E_d(0)R \exp\left(\frac{-K_d D}{\pi}\right) \exp\left[\frac{-c(D-z)}{\cos(\theta_v)}\right] \right] \quad (2)$$

where D is the water depth, z is the measurement depth, $E_d(0)$ is the downwelling irradiance just below the surface, and K_d is the downwelling diffuse attenuation. The first term in square brackets describes the radiance reflected off of the benthic surface, which for a Lambertian surface is uniform.

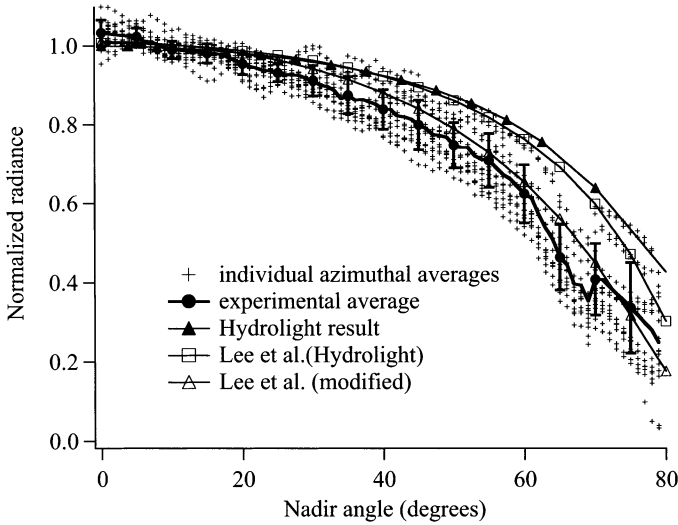


Fig. 4. Individual azimuthally averaged data at 440 nm (before 1800 UTC) shown as + along with average of this data and the Hydrolight model run for $\theta_o = 10^\circ$. Error bars on the experimental average are ± 1 standard deviation around the mean. The Petzold (1972) AUTEK phase function was used in these Hydrolight model runs. Two examples from the LSA model are also shown with input parameters identical to Hydrolight and modified slightly ($a(440 \text{ nm})$ adjusted from 0.054 m^{-1} to 0.074 m^{-1}) to fit the data.

The last exponential term describes the decrease in this radiance through the water column due to attenuation.

The first path radiance term, L_{bottom}^* , is due to light that has reflected off the bottom and then forward scattered (or multiply scattered) into the detector. Because this term involves the forward portion of the light scattering phase function, this can be a large term in the total radiance and has the effect of restoring some of the light scattered out of the direct component, L_{bottom} .

The last term, L_{surface}^* , is due to the light that is scattered into the viewing direction without interacting with the bottom. In optically deep water this term supplies the entire upwelling radiance, but in shallow water this term can be negligible.

With Hydrolight we can simulate specific cases that illustrate the different terms described above. To compare model and experimental results, we normalized each measured radiance distribution by the integrated radiance from 0 to 20° . For 440 nm we grouped the data into pre-1800 UTC and post-1800 UTC. In Figure 4 the individual data points, the azimuthal average of the data, and the azimuthal average of the Hydrolight result (for $\theta_o = 10^\circ$) are shown. The Hydrolight result at 10° was chosen because, for reasons discussed below, θ_o only significantly affects the magnitude of the upwelling radiance distribution, not its shape in this example. In Fig. 5 we present the data taken after 1800 UTC. In both of these examples the Hydrolight result is greater than the experimental results and can be accounted for by slight errors in the Hydrolight input data. In Fig. 6 the angular variation of the radiance distribution is shown along with the Hydrolight result for 670 nm, $\theta_o = 10^\circ$. The Hydrolight result qualitatively matches the experimental result very well, and at 670 nm (where pure water absorption is a dominant

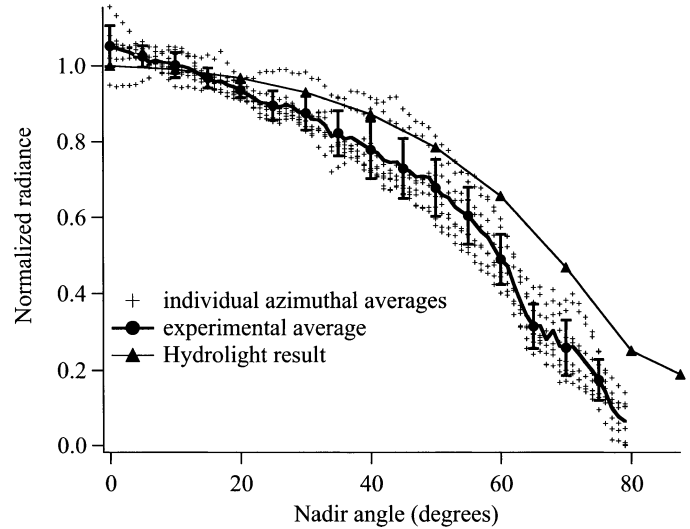


Fig. 5. Individual azimuthally averaged data at 440 nm (after 1800 UTC) shown as + along with average of this data and the Hydrolight model run for $\theta_o = 10^\circ$. Error bars on the experimental average are ± 1 standard deviation around the mean. The Petzold (1972) AUTEK phase function was used in the Hydrolight model run.

factor) the fit between the experiment and simulation is within the standard deviation of the measurements. Also shown in Figs. 4 and 6 are the results of using the semianalytic model of Lee et al. (1999) (referred to as LSA). If the same inputs are used in the Hydrolight simulations and LSA, the agreement is very good over almost the whole angular range. This may not be a totally surprising result since LSA was

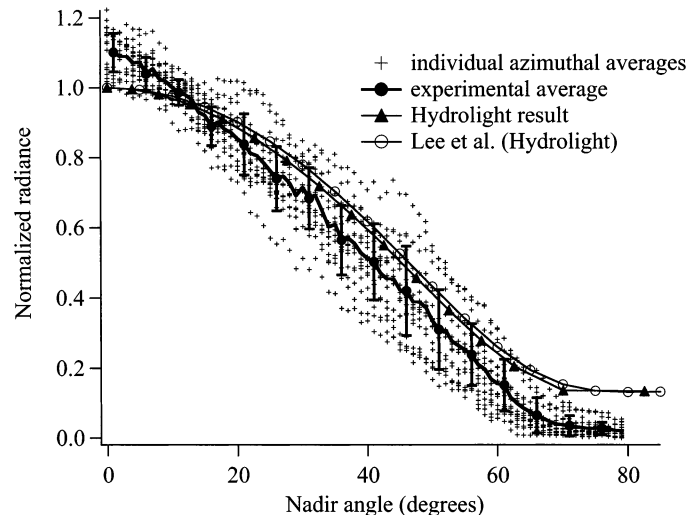


Fig. 6. Individual azimuthally averaged data at 670 nm shown as + along with average of this data and the Hydrolight model run for $\theta_o = 10^\circ$. Error bars on the experimental average are ± 1 standard deviation around the mean. The Petzold (1972) AUTEK phase function was used in these Hydrolight model runs. Agreement is good between the model and experiment. Because optical properties are dominated by pure water absorption, it is easier to have accurate inputs to the model.

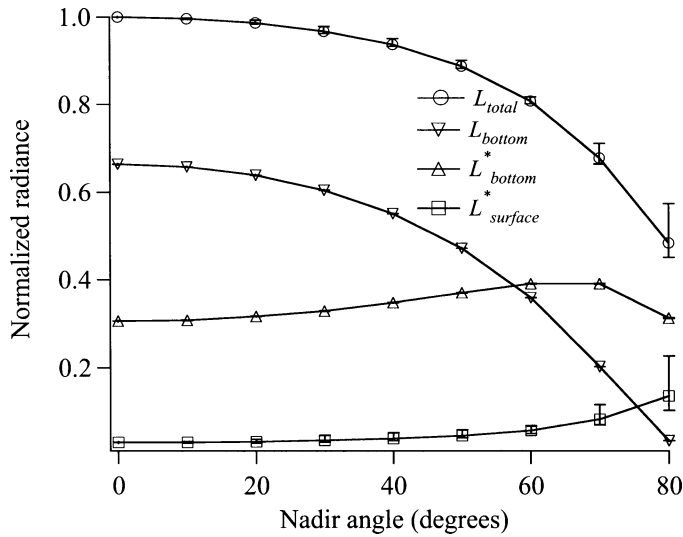


Fig. 7. Example of the magnitude of the components that make L_{total} . For this example, $\lambda = 440$ nm, $\theta_o = 60^\circ$, depth is 5 m, and the $R = 0.533$. As can be seen, $L_{surface}^*$ is negligible in this case. The strongest variation with θ_v comes from L_{bottom}^* .

based on simulations using Hydrolight. In Fig. 4, by varying the input to LSA (changing $a(440$ nm) from 0.054 to 0.074), better agreement can be found between the LSA and the experimental data. This illustrates that the difference between the Hydrolight simulation and the experimental data may simply be due to small errors in the input parameters, which were within the variations observed in the field.

By manipulating the input to the Hydrolight simulations, the importance of the various components in Eq. 1 can be determined. Hydrolight simulations were made with the $R = 0.0$. Since in this case there is no contribution due to light

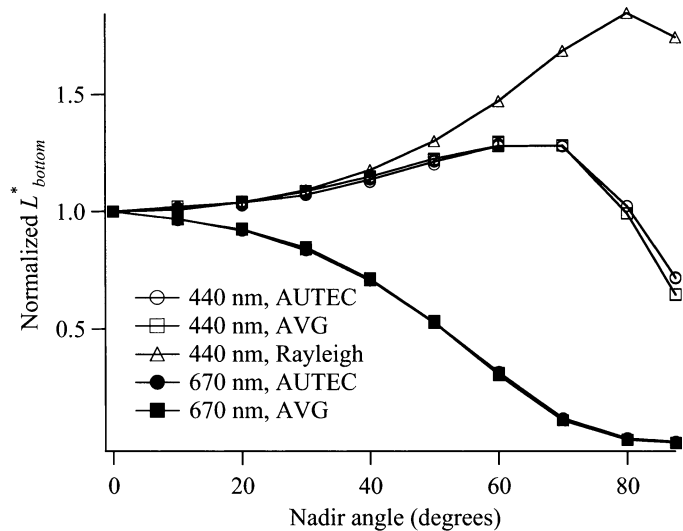


Fig. 8. Variation of L_{bottom}^* term, normalized at $\theta_v = 0^\circ$, with phase function. The two realistic phase functions give very similar results at 440 nm and 670 nm, however at 440 nm the Rayleigh like phase function gives a result that is significantly different. The higher $a(670$ nm) also causes a significant difference in the angular behavior of this term.

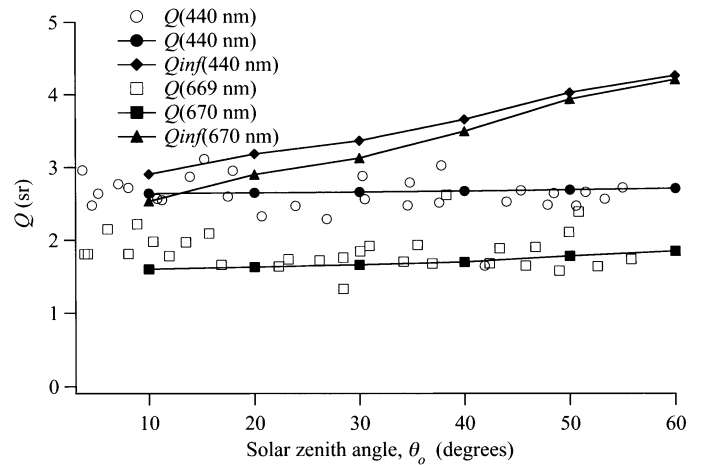


Fig. 9. Q as a function of solar zenith angle for experimental data (open symbols) and Hydrolight (filled symbols). Agreement between the model and data is good. The data are noisy because of wave focusing effects in L_u . Also shown is the Q for an infinite water column (Q_{inf}) for the two wavelengths and similar optical properties.

that has interacted with the bottom, this provides the $L_{surface}^*$ term described above. By using the downwelling irradiance at the benthic surface listed in the Hydrolight results, the bottom reflectance, and the beam attenuation, the L_{bottom} term can be determined. L_{bottom}^* can then be found by subtracting these two terms from L_{total} . The case of 440 nm and $\theta_o = 60^\circ$ is shown in Fig. 7. At each θ_v , Hydrolight calculates the radiance for 24 azimuth angles. The maximum, minimum, and mean are shown for each radiance parameter and θ_v . As can be seen, there is a variation in L_{total} with azimuth angle at the larger θ_v . However, the azimuthal dependence of L_{total} is contained in $L_{surface}^*$. $L_{surface}^*$ is strongly dependent on the light scattering phase function and the incident sky radiance distribution and is a small portion of L_{total} except at larger zenith angles. The shape of L_{bottom} and L_{bottom}^* are independent

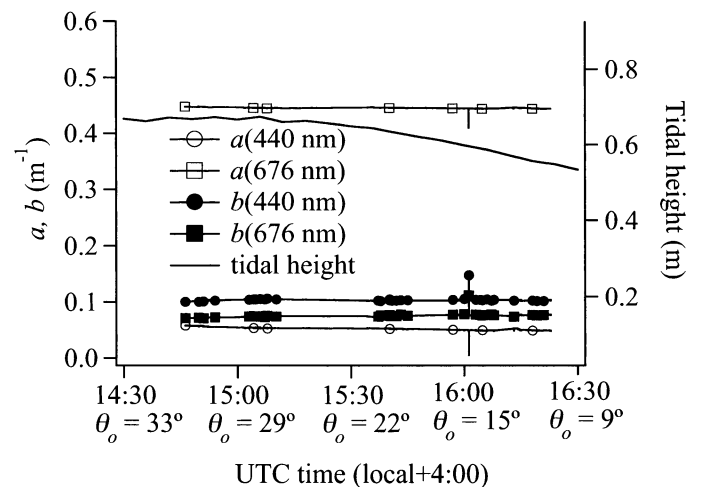


Fig. 10. Inherent water column optical properties throughout the measurement period of the seagrass site. Water properties were very constant during this period.

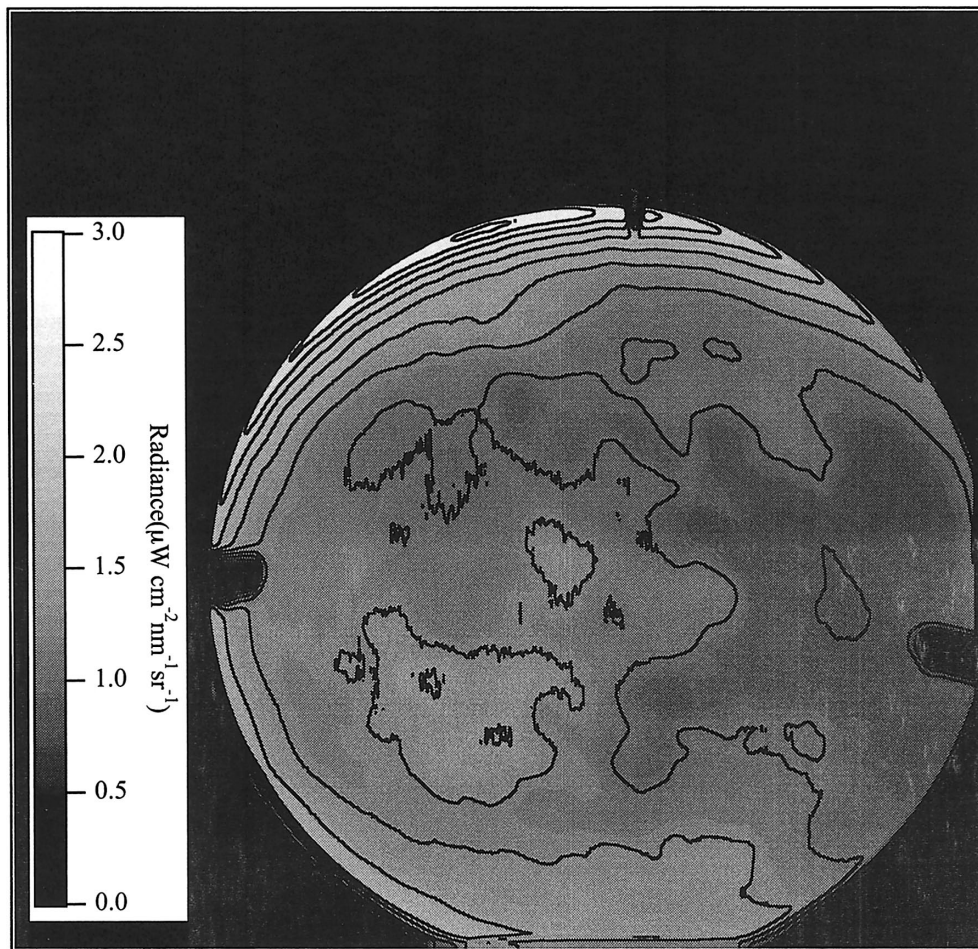


Fig. 11. Example radiance distribution above the seagrass bed. Environmental conditions were 440 nm, 1307 UTC (0907 local time), $\theta_o \approx 50^\circ$. The geometry of this image is the same as in Fig. 2, but the contour lines are at each $0.5 \mu\text{W cm}^{-2} \text{nm}^{-1} \text{sr}^{-1}$. Note that the radiance distribution is not azimuthally symmetric, but peaked toward the sun (upper left).

of the incident radiance distribution and θ_o , since their source is the diffuse bottom reflectance. Since L_{bottom} and L_{bottom}^* dominate L_{total} in this case, L_{total} has little dependence on θ_o . For $0^\circ < \theta_v < 40^\circ$, most important for remote sensing, the strongest variation with nadir angle is in the L_{bottom}^* .

The scattering phase function can affect the magnitude of L_{bottom} through its influence on the backscattering coefficient, b_b , and hence K_d , for the light that strikes the bottom and is reflected upward. Once the light has hit the benthic interface, transmission of L_{bottom} to the surface is governed by c . The path radiance terms can be influenced by the scattering phase function. To look at the variation of the L_{bottom}^* term, three phase functions were investigated, AUTEC, AVG, and for an extreme difference, a Rayleigh phase function. The variation of L_{bottom}^* with these phase functions is shown in Fig. 8. Here the L_{bottom}^* is normalized at $\theta_v = 0^\circ$ to offset magnitude variations due to K_d . In the range $0^\circ < \theta_v < 40^\circ$ there is little change in the L_{bottom}^* due to the phase function; however, after this angle the Rayleigh phase function does deviate significantly. A stronger variation in L_{bottom}^* occurs due to the single scattering albedo, however. On the same graph is shown the L_{bottom}^* for 670 nm, $\theta_o = 10^\circ$, and two scattering

phase functions (AUTEC and AVG). As seen, this is very different from the 440-nm result due to the extra absorption at 670 nm.

Q ($= E_u/L_u$, the ratio of the upwelling irradiance to the upwelling nadir radiance) is often used in remote sensing to relate the irradiance and radiance light fields. It is important because while the remote sensing signal is the upwelling radiance, the upwelling irradiance describes the upwelling energy flux through a surface. For a Lambertian surface, without attenuation, the Q above the surface would be π . For deeper water, Q seems to be limited to the range from 2.5 to 7, depending on the wavelength and optical characteristics of the water (Morel and Gentili 1996; Aas and Højerlev 1999; Zibordi and Berthon 2001). With our radiance distributions we can calculate Q directly. Since the scattering phase function has a weak effect on the angular variation of the upwelling radiance distribution over $0^\circ < \theta_v < 60^\circ$, one would expect that there would also be a small variation of Q due to the solar zenith angle. Figure 9 shows the Q calculated from the radiance data as a function of θ_o along with the Q calculated from the Hydrolight model. The Q calculated by Hydrolight for an infinitely deep water column is

also shown. As is seen, the Q from Hydrolight for shallow water is only weakly dependent on θ_o compared to the Q for deep water. The Q derived from the data is noisy. This is because Q is directly proportional to L_u , but the instantaneous L_u varies strongly due to wave focusing effects. In general the model and experiment agree. The radiance distributions are greatest at nadir; thus Q is significantly less than π , particularly at 440 nm. Obviously the effect of the benthic surface on Q needs to be taken into account when converting upwelling irradiance to upwelling radiance because significant errors could be introduced by assuming Q is π , or another deep water value.

Seagrass case—A seagrass experiment was performed to look at the effects of a lower reflectance benthic surface on the radiance distribution. This experiment was performed on 21 May 2000, at the seagrass closure site in North Rainbow Gardens (23° 47.51'N, 76° 08.33'W). In this case the water depth was approximately 9 m. This measurement was in the same channel as the sand case, so the same tidal effects occurred here. Figure 10 is a graph of the optical properties throughout the measurement period at this location. The optical properties of the water column were nearly constant over the measurement period. Figure 2 shows the spectral reflectance factor for the seagrass. This reflectance has more spectral features than seen in the sand; however, these features were fairly broad in this spectral range. In the seagrass case the reflectance of the bottom is not as large; hence, the benthic surface does not dominate the radiance distribution to the extent that the sand surface does. As an example we show Figure 11, an example of the seagrass radiance distribution, in this case 440 nm, 1307 UTC, at approximately $\theta_o = 50^\circ$. The geometry of this image is the same as in Fig. 3, but the contour lines are at each $0.5 \mu\text{W cm}^{-2} \text{nm}^{-1} \text{sr}^{-1}$. Bright and dark spots are still noticeable, but here these spots are a combination of wave focusing and the variations in the density of the seagrass. It is difficult to find a completely homogeneous seagrass bed. There were bright portions of the image that were stable over time from image to image, discounting wave focusing as the sole effect. As can be seen, the radiance distribution in this case is much more dependent on azimuthal angle (note the brightening toward the upper left).

Because the radiance distribution is less radially symmetric than the sand case we show the radiance, at 440 nm, along the plane 90° to the principal plane (the plane containing the nadir point and the antisolar point) in Fig. 12. This plane was chosen because the LSA model is specified for this plane. In each case two experimental measurements, bracketing the model θ_o , are shown. In these results, no normalization factor has been used. The model used two particulate scattering phase functions, the Petzold AUTEK phase function and the average particle phase function described above. The general shape of the 30° and 40° cases is much less dependent on θ_v than the sand case. The Hydrolight results also reflect this. The LSA model is also shown using the parameters of the Hydrolight AUTEK simulation. Hydrolight and LSA agree well between 0° and 40° ; however, after this the LSA model does not agree with either the experimental shape or the Hydrolight result. It should be

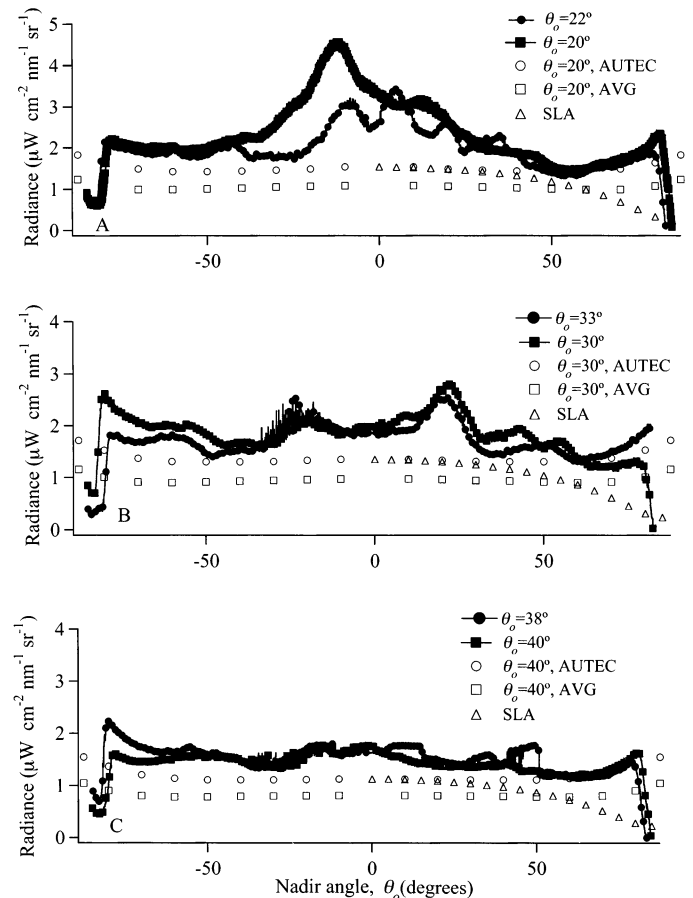


Fig. 12. Radiance in a plane 90° to the principal plane (plane containing nadir and antisolar point) for $\theta_o = 20^\circ, 30^\circ$, and 40° in the seagrass case at 440 nm. The open circles and open boxes are the Hydrolight results for the two scattering phase functions; the lines are two experimental results bracketing the model θ_o . These are unnormalized, absolute radiances from the model and experiment. Positive nadir angles are toward the sun. Also shown is the result from the LSA model with the same input parameters as the Hydrolight Autek simulation.

noted that Lee et al. (1999) indicate that LSA should not be used at $\theta_v > 40^\circ$. There is also a difference in the absolute magnitudes of the radiances between the data and model results. The data are almost always higher than the model results, even with the AUTEK scattering phase function, which has a strong backscattering component. To help show the importance of the terms making up the radiance distribution, an analysis (similar to that in Fig. 7) was performed and is shown in Fig. 13. For 440 nm, and $\theta_o = 60^\circ$, the L_{surface}^* term is the largest component of L_{total} , even at nadir. L_{bottom} is still one-fourth of L_{total} at nadir, but as the nadir angle increases, L_{surface}^* increasingly dominates. A similar analysis of the radiance distribution at 670 nm indicated that the L_{bottom} and L_{bottom}^* terms are negligible at all θ_v at this depth and benthic surface reflectance at 670 nm.

The overall magnitude of the difference between Hydrolight and the data at 440 nm could be attributed to an error in many of the parameters used as input to Hydrolight. However the difference between Hydrolight and the data for the

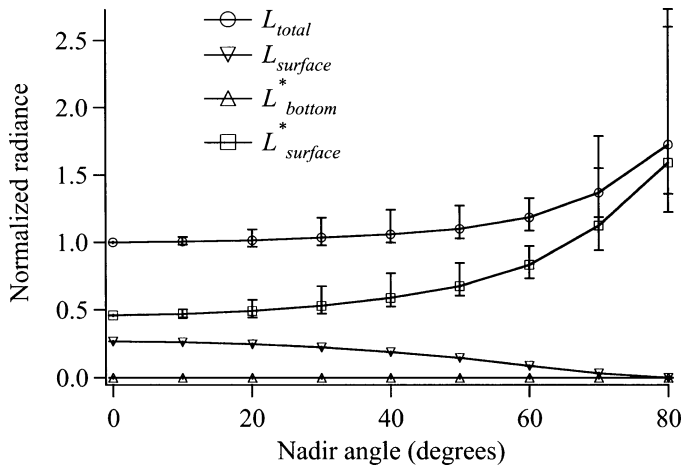


Fig. 13. Example of the magnitude of the components that make L_{total} . For this example, $\lambda = 440$ nm, $\theta_o = 60^\circ$, depth is 8 m, and $R = 0.051$. As can be seen, $L_{surface}^*$ is the largest contributor in this case.

different θ_o 's is interesting. While the general shape of the Hydrolight result and the data agree at large θ_o , as θ_o decreases the data starts to show a large change at small θ_o . This is most evident at $\theta_o = 20^\circ$. The angular variation of the data suggests that the model-data discrepancy is most likely due to the assumption that the seagrass is a homogeneous Lambertian reflector. Indeed, the seagrass canopy consists of leaves standing above a higher reflective substrate. When θ_o is small, it will strike the seagrass bed at an angle closer to the normal. In this case more light may be incident upon the substrate below the dark leaves, and when the radiance is viewed near normal, the brighter surface below the seagrass bed will be seen. As θ_o increases, more leaves are viewed; thus the apparent reflectance (and radiance) decreases.

For the cases with larger θ_o , the light is incident on the seagrass bed at a greater angle; thus more light is incident on the leaves, and less makes it to the brighter subsurface. Note that the progression appears to be that the agreement between the model and the data improves with increasing θ_o . This is probably due to a decreasing influence of the substrate below the seagrass canopy.

We have not shown the results at 670 nm in the seagrass case. As discussed above, at this wavelength the upwelling radiance distribution is dominated by $L_{surface}^*$ and is thus not an optically shallow case. The comparison becomes a study of phase function effects such as discussed in Mobley et al. (2002) and is outside the scope of this paper.

When investigating the Q above this surface, we find that Q is much more dependent on θ_o , increasing with increasing θ_o (Fig. 14). Both the data and the model have this trend, although the data are significantly different than the model, in particular for 440 nm and small θ_o . Here the BRDF effects, discussed above, decrease Q (440 nm) in the experimental data is still noisy because L_u in the denominator increases when wave focusing causes a bright spot at nadir. Overall, Q is much larger over seagrass than over the bright sand and closer to the open water values.

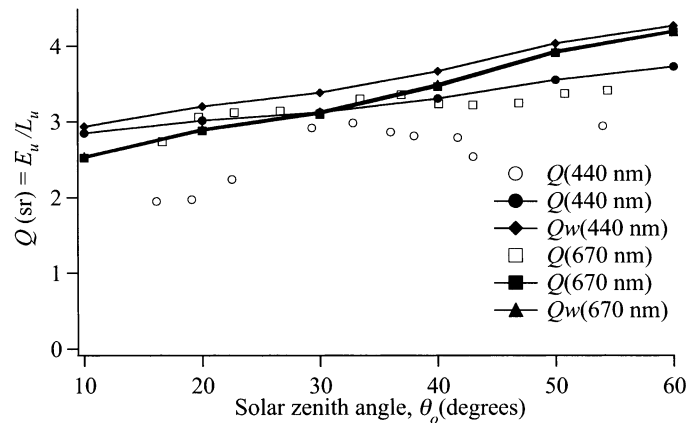


Fig. 14. Q as a function of θ_o for the seagrass case. As can be seen there is a strong dependence of Q on θ_o . Also Q is much larger than in the bright sand condition, and closer to the optically deep water column case.

References

- AAS, E., AND N. K. HOJERSLEV. 1999. Analysis of underwater radiance observations: Apparent optical properties and analytical functions describing the angular radiance distribution. *J. Geophys. Res.* **104**: 8015–8024.
- GORDON, H. R., AND O. B. BROWN. 1974. Influence of bottom depth and albedo on the diffuse reflectance of a flat homogeneous ocean. *Appl. Opt.* **13**: 2153–2159.
- JERLOV, N. G. 1976. *Marine Optics*. Elsevier.
- JOSEPH, J. 1950. Untersuchungen über Ober- und Unterlichtmessungen im Meere und über ihren Zusammenhang mit Durchsichtsmessungen. *Dtsch. Hydrogr. Z.* **3**: 324–335.
- LEE, Z., K. L. CARDER, C. D. MOBLEY, R. G. STEWARD, AND J. S. PATCH. 1998. Hyperspectral remote sensing for shallow waters. I. A semianalytic model. *Appl. Opt.* **37**: 6329–6337.
- , ———, ———, ———, AND ———. 1999. Hyperspectral remote sensing for shallow waters. 2. Deriving bottom depths and water properties by optimization. *Appl. Opt.* **38**: 3831–3843.
- MARITORENA, S., A. MOREL, AND B. GENTILI. 1994. Diffuse reflectance of oceanic shallow waters: Influence of water depth and bottom albedo. *Limnol. Oceanogr.* **39**: 1689–1703.
- MAZEL, C. H. 1997. Diver-operated instrument for in situ measurement of spectral fluorescence and reflectance of benthic marine organisms and substrates. *Opt. Eng.* **36**: 2612–2617.
- MOBLEY, C. D. 1994. *Light and water*. Academic.
- , AND OTHERS. 1993. Comparison of numerical models for computing underwater light fields. *Appl. Opt.* **32**: 7484–7504.
- , AND L. K. SUNDMAN. 2000a. *Hydrolight 4.1 users' guide*. Sequoia Scientific.
- , AND ———. 2000b. *Hydrolight 4.1 Technical Documentation*. Sequoia Scientific.
- , ———, AND E. BOSS. 2002. Phase function effects on the oceanic light fields. *Appl. Opt.* **41**: 1035–1050.
- , H. ZHANG, AND K. J. VOSS. 2003. Effects of optically shallow bottoms on upwelling radiances: Bidirectional reflectance distribution function effects. *Limnol. Oceanogr.* **48**: 337–345.
- MOREL, A., AND B. GENTILI. 1996. Diffuse reflectance of oceanic waters. III. Implication of bidirectionality for the remote-sensing problem. *Appl. Opt.* **35**: 4850–4862.
- PETZOLD, T. J. 1972. *Volume scattering functions for selected ocean waters*. Scripps Institution of Oceanography.
- PLASS, G. N., AND G. W. KATTAWAR. 1972. Monte Carlo calcula-

- tions of radiative transfer in the Earth's atmosphere-ocean System: I. Flux in the atmosphere and ocean. *J. Phys. Oceanogr.* **2**: 139–145.
- SMITH, R. C., R. W. AUSTIN, AND J. E. TYLER. 1970. An oceanographic radiance distribution camera system. *Appl. Opt.* **9**: 2015–2022.
- VOSS, K. J. 1989. Electro-optic camera system for measurement of the underwater radiance distribution. *Opt. Eng.* **28**: 241–247.
- , AND A. L. CHAPIN. 1992. Next generation in-water radiance distribution camera system. *Proc. Soc. Photo-Optical Instrumentation Engineers* **1750**: 384–387.
- WET LABS 2000. Ac-9 Protocol Revision D. Wet Labs.
- ZANEVELD, J. R. V., AND E. BOSS. 2003. The influence of bottom morphology on reflectance: Theory and two-dimensional geometry model. *Limnol. Oceanogr.* **48**: 374–379.
- ZHANG, H., K. J. VOSS, R. P. REID, AND E. LOUCHARD. 2003. Bidirectional reflectance measurements of sediments in the vicinity of Lee Stocking Island, Bahamas. *Limnol. Oceanogr.* **48**: 380–389.
- ZIBORDI, G., AND J.-F. BERTHON. 2001. Relationships between Q-factor and seawater optical properties in coastal region. *Limnol. Oceanogr.* **46**: 1130–1140.

Received: 17 September 2001

Accepted: 31 May 2002

Amended: 12 June 2002